Journal of Aerosol Science 83 (2015) 39–54

Contents lists available at ScienceDirect

Journal of Aerosol Science

journal homepage: www.elsevier.com/locate/jaerosci

# Particle effective density and mass during steady-state operation of GDI, PFI, and diesel passenger cars

David C. Quiros [a,b,*], Shaohua Hu [a], Shishan Hu [c], Eon S. Lee [d], Satya Sardar [c], Xiaoliang Wang [e], Jason S. Olfert [f], Heejung S. Jung [g], Yifang Zhu [b,d], Tao Huai [a,d]

[a] Monitoring and Laboratory Division, California Air Resources Board, 1900 14th Street, Sacramento, CA 95811, USA
[b] Environmental Science & Engineering, Institute of the Environment and Sustainability, University of California, Los Angeles, La Kretz Hall, Suite 300, Los Angeles, CA 90095-1496, USA
[c] Emissions Compliance, Automotive Regulations and Science Division, California Air Resources Board, 9528 Telstar Avenue, El Monte, CA 91731, USA
[d] Environmental Health Sciences, Fielding School of Public Health, University of California, Los Angeles, 650 Charles E. Young Drive South, Los Angeles, CA 90095, USA
[e] Division of Atmospheric Sciences, Desert Research Institute, 2215 Raggio Parkway, Reno, NV 89512, USA
[f] Department of Mechanical Engineering, University of Alberta, 5-1C Mechanical Engineering Building, Edmonton, Alberta, Canada T6G 2G8
[g] Center for Environmental Research and Technology (CE-CERT), Bourns College of Engineering, University of California, Riverside, 1084 Columbia Avenue, Riverside, CA 92507, USA

ARTICLE INFO

*Article history:*
Received 23 August 2014
Received in revised form
2 December 2014
Accepted 15 December 2014
Available online 23 December 2014

*Keywords:*
LEV III
Particulate matter
Effective density
Centrifugal particle mass analyzer
Particle size distribution

ABSTRACT

Particle effective density is an important physical property of vehicle exhaust, and is required for estimating particulate matter (PM) mass emissions using the Integrated Particle Size Distribution (IPSD) method. In this study, we measure particle effective density of five light-duty vehicles with PM emissions below the Low Emission Vehicle (LEV) III PM standards of 1 or 3 mg/mi (0.62 and 1.86 mg/km) using the Differential Mobility Analyzer (DMA) – Centrifugal Particle Mass Analyzer (CPMA) approach. Test vehicles included two gasoline direct injection (GDI) vehicles without particulate filters, and for the first time reported in the literature, two port-fuel injected (PFI) vehicles and a turbocharged direct injection (TDI) light-duty diesel vehicle with a diesel particulate filter (DPF). The particle effective density functions generally resemble previous work on GDI and diesel engines without particulate filters but, for many size ranges, the PFI and TDI vehicles produced emissions with higher particle effective densities than GDI vehicles. Good linear correlation was found between the gravimetric and IPSD methods when applying the new particle effective density functions to size distribution measured by the TSI Engine Exhaust Particle Sizer (EEPS, 5.6–560 nm, $R^2=0.84$); however, the IPSD method underestimated gravimetric mass by 64%. When using a TSI Aerodynamic Particle Sizer (APS, 0.54–2.5 μm) to measure the contribution of larger particles, underestimation bias was virtually eliminated and the correlation improved dramatically ($R^2=0.96$). Even stronger correlation between IPSD and gravimetric methods was achieved when using a Scanning Mobility Particle Sizer (SMPS, 8.7–365 nm) and the APS ($R^2=0.97$). A procedure for correcting EEPS measurements using the SMPS is presented and evaluated.



* Corresponding author at: Monitoring and Laboratory Division, California Air Resources Board, 1900 14th Street, Sacramento, CA 95811, USA. Tel.: +1 916 445 9370; fax: +1 916 324 1556.
*E-mail address:* dquiros@arb.ca.gov (D.C. Quiros).

http://dx.doi.org/10.1016/j.jaerosci.2014.12.004
0021-8502/

## 1. Introduction

Exposure to particulate matter (PM) is associated with increased cardiopulmonary morbidity and mortality (Pope & Dockery, 2006) and is influenced by mobile source emissions (EPA, 2002; Hill et al., 2009; Lloyd & Cackette, 2001). The California Air Resources Board (ARB) recently adopted the Low Emissions Vehicle (LEV) III regulations which, by 2025, will reduce the light-duty vehicle PM emission standards for the Federal Test Procedure (FTP) from 10 to 3 and ultimately to 1 mg/mi (6.2–0.62 mg/km) (CARB, 2012a). Recently, ARB and U.S. EPA demonstrated measurement of PM emissions below 1 mg/mi (0.62 mg/km) using the existing filter-based gravimetric method (Hu et al., 2014). However, alternative measurement approaches are still of great interest to better understand the characteristics of PM at very low levels.

One alternative method for PM mass measurement is the Integrated Particle Size Distribution (IPSD) method, a phrase first used by Liu et al. (2009) referring to the general method for estimating PM concentrations from particle size distribution and effective density. Defined as mass divided by electrical mobility equivalent volume (Kelly & McMurry, 1992), particle effective density enables rapid conversion between number and mass distributions, or between mobility and aerodynamic diameters, without assuming bulk density or morphology. Several studies have reported particle effective density of emissions from gasoline, natural gas, and diesel engines (e.g. Barone et al., 2011; Bullock & Olfert, 2014; Maricq & Xu, 2004; Olfert, Symonds, & Collings, 2007; Park, Cao, Kittelson, & McMurry, 2003; Ristimäki, Virtanen, Marjamäki, Rostedt, & Keskinen, 2002; Van Gulijk, Marijnissen, Makkee, Moulijn, & Schmidt-Ott, 2004; Virtanen, Ristimäki, Vaaraslahti, & Keskinen, 2004; Zelenyuk, Cai, Chieffo, & Imre, 2005). Except for one study reporting constant effective density of emissions from a natural gas engine (Bullock & Olfert, 2014), the majority of studies on gasoline and diesel engines show particle effective density decreases as a function of particle size, in general agreement with the power fit model for fractal aerosols using a mass–mobility scaling exponent (Sorensen, 2011). However, to the best of our knowledge, only one study has evaluated gasoline direct injection (GDI) emissions (i.e. Maricq & Xu, 2004), and no previous studies have measured particle effective density from port-fuel injected (PFI) gasoline or light-duty diesel vehicles equipped with a diesel particulate filter (DPF). Therefore, redefining the particle effective density functions over the breadth of current vehicle technologies is needed to properly evaluate IPSD.

Kelly and McMurry (1992) first measured effective density of laboratory aerosol using a Differential Mobility Analyzer (DMA) and an inertial cascade impactor. Subsequently, several studies used a DMA placed upstream of an Electrical Low Pressure Impactor (ELPI, Ahlvik, Ntziachristos, Keskinen, & Virtanen, 1998; Keskinen, Pietarinen, & Lehtimäki, 1992; Maricq, Podsiadlik, & Chase, 2000; Maricq & Xu, 2004) providing real-time aerodynamic size distribution for a given DMA set point. A DMA has also been operated as part of a Scanning Mobility Particle Sizer (SMPS) in parallel to, rather than in series with, an ELPI for making density measurements more quickly by fitting size distributions (Ristimäki et al., 2002; Virtanen, Ristimäki, & Keskinen, 2004; Virtanen et al., 2002). A DMA has also been placed upstream of an Aerosol Particle Mass Analyzer (APM, Ehara, Hagwood, & Coakley, 1996) and Centrifugal Particle Mass Analyzer (CPMA, Olfert & Collings, 2005), which both classify according to mass to charge ratio using two rotating concentric cylinders to balance electrostatic and centrifugal forces. McMurry, Wang, Park, and Ehara (2002) used a DMA and APM to measure the effective density of atmospheric aerosol, and the approach has been subsequently applied to characterize engine exhaust particles (e.g. Barone et al., 2011; Park et al., 2003). Later, the CPMA was designed to improve the transfer function of the APM by using slightly different angular velocities for the two rotating cylinders (Olfert & Collings, 2005; Olfert, Reavell, Rushton, & Collings, 2006). There are other methods for measuring particle effective density, such as using a DMA and Single Particle Laser Ablation Time-of-flight Mass Spectrometer (SPLAT, Zelenyuk et al., 2005). However, the system measures vacuum aerodynamic diameter and has low ($<0.1\%$) detection efficiencies for particles below 50 nm (Zelenyuk, Yang, Choi, & Imre, 2009) and is not commercially available. The Dekati Mass Monitor (DMM, Lehmann, Niemelä, & Mohr, 2004) uses yet another approach by combining one mobility with six aerodynamic channels measuring size distribution to estimate particle effective density in real time. The DMM is used widely to measure PM mass, but density values are not reported but are used to directly report mass concentration based on a unimodal size distribution, mass median diameter, and geometric standard deviation (GSD), which have all shown to largely deviate from accepted reference methods (Mamakos, Ntziachristos, & Samaras, 2006; Quiros et al., 2014).

In this study, we use the DMA–CPMA method to measure particle effective density from two gasoline direct injected (GDI-1 and GDI-2) and two port fuel injected (PFI and PFI-E85) gasoline vehicles, and one turbo direct injection (TDI) light-duty diesel vehicles on a chassis dynamometer. Because the DMA–CPMA approach requires several minutes to complete each measurement, steady-state testing was conducted. The primary objective of this study was to determine particle effective density functions that can be used to evaluate the capability of IPSD to estimate PM mass emitted from light-duty vehicles meeting the LEV III standards. A secondary objective is to compare size distributions measured by the TSI Engine Exhaust Particle Sizer (EEPS, 5.6–560 nm) and SMPS (8.7–365 nm). The SMPS is regarded as the reference method for measuring size distribution; however, it requires one to two minutes to complete a scan, and therefore the EEPS was developed to measure transient particle size distributions. Therefore, SMPS-to-EEPS ratio is calculated under controlled steady-state conditions, and is used to correct EEPS measurements. Finally, this study also aims to measure the contribution of larger particle sizes using a TSI Aerodynamic Particle Sizer (APS, 0.54–2.5 μm), in order to compare total suspended real-time mass with the filter-based gravimetric standard method.

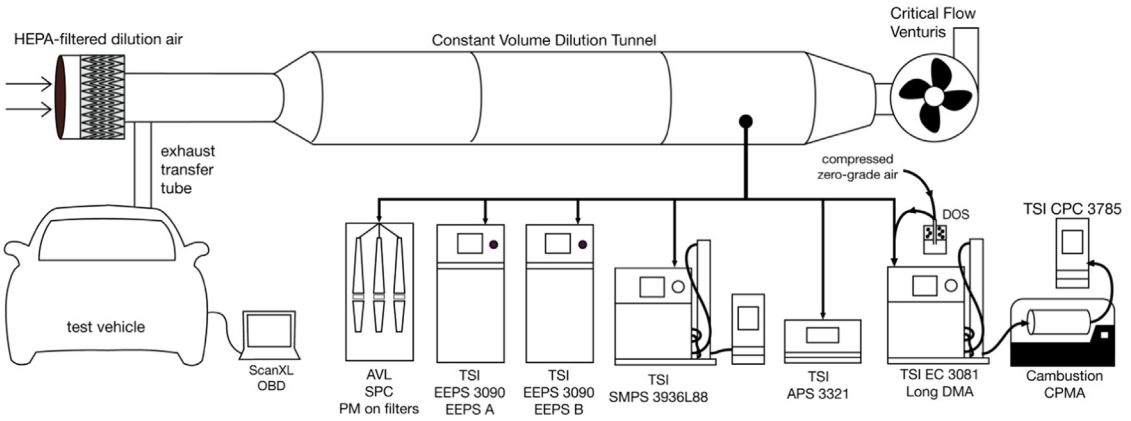


**Fig. 1.** Schematic of laboratory and instrument setup.

## 2. Methods

### 2.1. Laboratory, instruments, and quality assurance

All data were collected at ARB's Haagen-Smit Laboratory (HSL) in El Monte, CA in one of the light-duty test cells equipped with a 48-in. single-roll electric chassis dynamometer, a constant volume sampler (CVS), and sampling systems meeting certification requirements defined by 40 CFR 1066 (U.S. EPA, 2012). A cyclone upstream of all PM sampling was used to remove particles larger than 2.5 μm, an optional requirement listed in the CFR.

Figure 1 shows the instrumentation and sampling setup. The real-time PM instrumentation included two (Units A and B) TSI Engine Exhaust Particle Sizers (EEPS 3090, 5.6–560 nm, Firmware MCU 3.11 DSP 3.02, TSI Inc., Shoreview, MN, USA) both operating with a 1-s sampling interval, a TSI Scanning Mobility Particle Sizer 3936L88 (SMPS, 8.7–365 nm) operating at a 2-min time resolution (upscan 100 s, downscan 20 s), a TSI Aerodynamic Particle Sizer 3321 (APS, 0.54–19.81 μm) operating at a 5-s time resolution, and the DMA–CPMA setup with the TSI Long DMA (model 3081, Shoreview, MN) and Cambustion CPMA (Cambustion Ltd, Cambridge, United Kingdom).

The CPMA was calibrated by the manufacturer immediately prior to the study where angular velocity and voltages were within 3% and 5%, respectively, of relevant international standards, indicating good system functionality for classifying particle mass (Symonds, Reavell, & Olfert, 2013). The overall uncertainty of the method may be up to 9.4% (Johnson, Symonds, & Olfert, 2013); however, the actual uncertainty of particle effective density measurement has been shown to be about 3% (Olfert et al., 2006). To verify proper system function, dioctyl sebacate (DOS) spheres were generated to compare measured density with the bulk density (917 kg/m$^3$) for spherical laboratory particles. DOS aerosol was generated using a 0.05% volume solution DOS in HPLC-grade 2-propanol at 18 PSI using a triple-jet nebulizer that is based on the original design by W.H. Collison (BGI model MRE CN24/25, Waltham, MA), and a dilution ratio of 300. The ranges of calculated densities agreed with reference material density, where coefficient of variation ranged between 1.6% and 10% for all sizes. Some uncertainty may have been caused by evaporation of the test aerosol in the DMA after dilution with the sheath flow, the residence time in the short tubing between the DMA and CPMA, or evaporation within the classification space of CPMA. The difference between measured and bulk DOS density remained below the 9.4% uncertainty except for measurements made at 30 nm that exhibited a 19% difference. The classification of smaller particles in the CPMA requires higher rotational speed and greater centrifugal force, but such forces have no relevant impact on pressure in the classification space affecting the state of volatile particles. Higher rotational speeds can result in slightly warmer temperature (by approximately 10–20 °C above ambient), and some evaporation may have occurred, especially at 30 nm because of the increased vapor pressure described by the Kelvin effect for smaller particles with stronger surface curvatures. Importantly, the accuracy and precision of the DMA–CPMA remained constant and no performance drift was observed over the duration of the test program.

Prior to the study, the SMPS and the DMA used with the CPMA were challenged by particles with diameters between 30 and 240 nm that were selected by a third reference DMA. The reference DMA was calibrated to standard polystyrene latex (PSL, Thermo Fisher Scientific, Waltham, MA, USA) spheres and was not used for experimental measurement. The average size discrepancy between reference and challenge instruments was 2% for the DMA used in tandem with the CPMA and 4% for the DMA used for the SMPS, suggesting good calibration of sample flows from the CPC and the sheath flows controlled by the TSI electrostatic classifier units. The two CPCs were checked daily for leaks by ensuring a zero reading when measuring particle-free air. Similarly, the two EEPS were challenged for verification using the reference DMA; depending on particle size, error between 5% and 40% was calculated for either unit. The discrepancy between DMA and EEPS sizing is of notable concern and is discussed as a key objective of this paper. EEPS electrodes were cleaned prior to the study using the provided acrylic cylinder and lint-free cloth, and charging needles were cleaned using forceps. Each day before testing, the units were

**Table 1**
Vehicles used to measure density and PM mass using IPSD over steady-state cycles.

| ID | Fuel | Model year | Make/model | Engine | CA emissions level | Emissions technologies | PM FTP (mg/mi (/km)) | Mileage ($10^3$) km |
|---|---|---|---|---|---|---|---|---|
| GDI-1 | E10 | 2013 | Ford Focus | 2.0-L GDI | SULEV II | TWC | 0.99 (0.61) | 49.2 |
| GDI-2 | E10 | 2014 | Chevrolet Traverse | 3.6-L GDI | ULEV II | TWC | 2.02 (1.23) | 23.1 |
| PFI | E10 | 2012 | Chevrolet Malibu | 2.4-L PFI | ULEV II | TWC | 0.29 (0.18) | 43.4 |
| PFI-E85 | E85 | 2008 | Chevrolet Impala | 3.5-L PFI | ULEV II | TWC | 0.10 (0.06) | 92.1 |
| TDI | ULSD | 2013 | Volkswagen Passat | 2.0-L TDI | ULEV II | DOC, DPF, SCR, EGR, TC | 0.11 (0.07) | 0.32 |

PFI=port fuel injection, GDI=gasoline direct injection, TDI=turbo direct injection, TWC=three way catalyst, DOC=diesel oxidation catalyst, DPF=diesel particulate filter, SCR=selective catalytic reduction, EGR=exhaust gas recirculation, TC=turbocharger.

warmed up for at least one hour, the electrometers were zeroed, and electrometer offset and noise values were recorded; the cleaning procedure was repeated once for both instruments during the study using the acrylic cylinder when offset readings exceeded a 20-fA threshold. The response of the two EEPS was averaged, although during a few tests only one instrument reported usable data.

PM mass was measured using the regulatory method by collection onto 47-mm Teflon filters (2-μm pore size, Whatman) heated to $47 \pm 5$ °C at a filter face velocity of approximately 90 cm/s using an AVL Smart Sampler (model SPC 478). Filters were handled and weighed following ARB Standard Operating Procedure for the Determination of Particulate Matter (PM) Mass Collected On Filters (SOP no. MLD145), which has specifications for charge neutralization, buoyancy correction, temperature and humidity control, and an ISO Class 6 weigh room (CARB, 2012b). Quality control and assurance checks were performed on the laboratory CVS and PM sampling equipment on a weekly basis to ensure compliance with 40 CFR parts 86 and 1066 standards for regulated pollutants (U.S. EPA, 2001, 2012).

### 2.2. Vehicles and testing conditions

Table 1 describes the five vehicles tested by engine size, type, PM emission rates over the FTP, key emission control technologies, and mileage. Two late model year vehicles with GDI engines were selected to evaluate particle effective density as a function of smaller engine size (2.0 L, GDI-1) to larger engine size (3.6 L, GDI-2). Two vehicles with PFI engines were evaluated, one operating on standard fuel (PFI), the other a Flex-fuel engine operating on commercially available E-85 (PFI-E85). The fifth vehicle (TDI) was operated on ultralow sulfur diesel and was equipped with a diesel oxidation catalyst, DPF, and selective catalytic reduction system. The TDI was procured and tested with low accumulated mileage ($< 320$ km), which implies that the repression of stored sulfur from catalyzed after treatment may be more limited compared to vehicles later during useful life, and therefore effective density values may differ as a function of vehicle age (Herner et al., 2011; Swanson, Kittelson, Watts, Gladis, & Twigg, 2009; Zheng et al., 2011).

Table 2 lists the operating conditions of each test vehicle by engine power (kW). Each power target is labeled with the percentile (%) of time the FTP test demands a vehicle power less than the value, which was calculated using target dynamometer coefficients and the FTP speed–time trace. In this paper, all parameters are reported relative to work at the engine (target coefficients), which is the sum of the dynamometer power (set coefficients) and internal mechanical resistance. Vehicle wheel speeds ranged from 40 to 120 km/h, and a simulated road grade between 0% and 2.5% was applied to obtain desired engine power and torque parameters. A 15-min warm-up period preceded each 75-min test to warm up the engine, catalyst, exhaust manifold, and exhaust transfer tube. Each condition was repeated between two to four times, resulting in over 60 h of data collected in the study.

Figure 2 illustrates the two testing configurations used in this study: steady-state with constant speed (SS), and steady-state with a simulated transient (ST) operation. During ST operation, the driver was instructed to modulate the accelerator every 6 s to vary the wheel speed within a $\pm 3$ km/h range of the target driving speed. Experimental data indicate peak acceleration typically ranged between 5 and 6 km/h-s (3.1 and 3.8 mi/h-s) during ST operation. This approach was used to introduce some aspects of transient operation such as changes in the injected fuel quantity and spark timing while maintaining the same average power as SS operation. Furthermore, the ST operation generated higher particle concentrations for lower loads of the PFI and TDI vehicles. At the point of density measurement, sufficient axial dispersion had occurred so that particle concentrations were constant. Although effective density measured during ST operation may exhibit some characteristics of transient operation induced during certification test cycles, it does not account for some conditions such as cold-start, or emissions during deceleration periods.

### 2.3. DMA–CPMA operation and analysis

Effective density was determined at seven set points between the lower boundary of interest and upper detection limit, at 30, 55, 90, 140, 210, 270, and 350 nm. The CMPA was operated with a constant transfer function, with a resolution

**Table 2**
Test operating conditions defined by engine power (kW), engine torque (N m), and engine speed (rpm). Power percentages in parentheses reflect the percentile of the power of each vehicle during a transient FTP certification test. SS and ST refer to steady-state and simulated transient operations, respectively, which are illustrated in Fig. 2. Mass–mobility scaling exponent and density constant data (Eq. (4)) are reported as ± one standard deviation.

| Vehicle | Condition 1 | Condition 2 | Condition 3 | Condition 4 | Condition 5 |
|---|---|---|---|---|---|
| *GDI-1* | *SS* | *SS* | *SS* | | |
| Power (kW) | 6.5 (48%) | 16 (89%) | 30 (99.5%) | | |
| Torque (N m) | 40 | 81 | 107 | | |
| Speed (rpm) | 1550 | 1900 | 2650 | | |
| Dilution ratio | 13.3 | 8.6 | 5.5 | | |
| *Exponent*, $D_m$ | 2.44 ± 0.06 | 2.45 ± 0.08 | 2.32 ± 0.07 | | |
| *Constant*, $c$[a] | 5.9 ± 1.8 | 6.3 ± 2.2 | 11 ± 3.7 | | |
| *GDI-2* | *SS* | *SS* | *SS* | *SS* | *SS* |
| Power (kW) | 9.0 (42%) | 9.0 (42%) | 26 (91%) | 26 (91%) | 51 (99.7%) |
| Torque (N m) | 67 | 33 | 188 | 100 | 180 |
| Speed (rpm) | 1250 | 2600 | 1350 | 2500 | 2650 |
| Dilution ratio | 10.1 | 7.7 | 5.8 | 5.2 | 6.3 |
| *Exponent*, $D_m$ | 2.52 ± 0.00 | 2.40 ± 0.01 | 2.47 ± 0.05 | 2.40 ± 0.04 | 2.29 ± 0.08 |
| *Constant*, $c$[a] | 4.5 ± 0.4 | 6.2 ± 0.5 | 5.5 ± 0.9 | 7.1 ± 1.1 | 17 ± 6.3 |
| *PFI* | *ST* | *ST* | *SS* | | |
| Power (kW) | 5.4 (32%) | 14 (78%) | 18 (88%) | | |
| Torque (N m) | 35 | 89 | 110 | | |
| Speed (rpm) | 1500 | 1500 | 1500 | | |
| Dilution ratio | 9.4 | 6.9 | 8.0 | | |
| *Exponent*, $D_m$ | 2.68 ± 0.06 | 2.45 ± 0.08 | 2.67 ± 0.08 | | |
| *Constant*, $c$[a] | 2.2 ± 0.7 | 7.0 ± 2.7 | 2.5 ± 1.1 | | |
| *PFI-E85* | *ST* | *ST* | *SS* | | |
| Power (kW) | 6 (40%) | 16 (84%) | 16 (84%) | | |
| Torque (N m) | 38 | 120 | 120 | | |
| Speed (rpm) | 1500 | 1300 | 1300 | | |
| Dilution ratio | 10.4 | 6.5 | 7.8 | | |
| *Exponent*, $D_m$ | 2.52 ± 0.07 | 2.42 ± 0.10 | 2.39 ± 0.03 | | |
| *Constant*, $c$[a] | 3.8 ± 1.3 | 5.9 ± 3.0 | 7.3 ± 1.0 | | |
| *TDI* | *SS* | *SS* | *ST* | *Regeneration* | |
| Power (kW) | 12 (87%) | 16 (93%) | 16 (93%) | 16 (93%) | |
| Torque (N m) | 100 | 100 | 100 | 100 | |
| Speed (rpm) | 1150 | 1550 | 1550 | 1500 | |
| Dilution ratio | 5.6 | 6.8 | 6.3 | 6.8 | |
| *Exponent*, $D_m$ | 2.96 ± 0.04 | 2.59 ± 0.02 | 2.59 ± 0.07 | 2.68 ± 0.03 | |
| *Constant*, $c$[a] | 1.7 ± 0.3 | 3.9 ± 0.3 | 7.9 ± 2.6 | 2.4 ± 1.1 | |

[a] Following the exponential decay function in the following form given by Eq. (4).

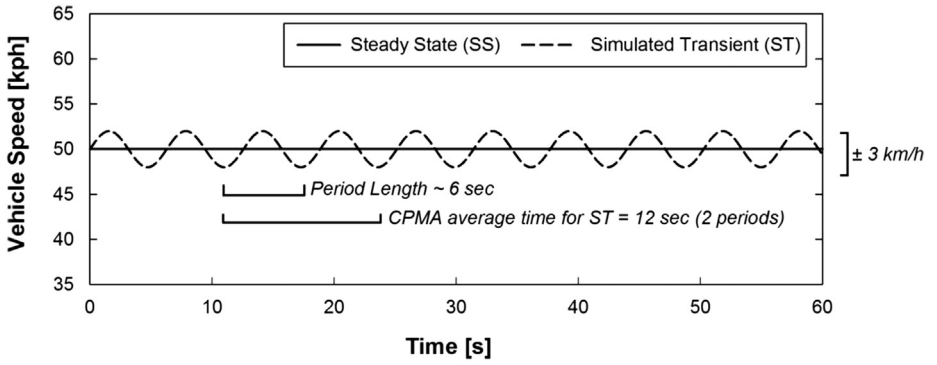


**Fig. 2.** Illustrative comparison of the Steady State (SS) versus Transient Throttling (ST) operation modes at a vehicle speed of 50 km/h.

parameter $R_m$ between 5 and 10 (the inverse of the full width half maximum of the transfer function normalized by the mass set point), and with an averaging time of 4 s for SS operation, and 12 s for ST operation (Fig. 2). When using a CPC 3785 aerosol flow rate of 1.0 L/min and collecting between 15 and 30 points per scan, each scan required 8–12 min. The first and last CPMA scans were made at the same DMA set point to verify density did not change for that size over the 75-min test

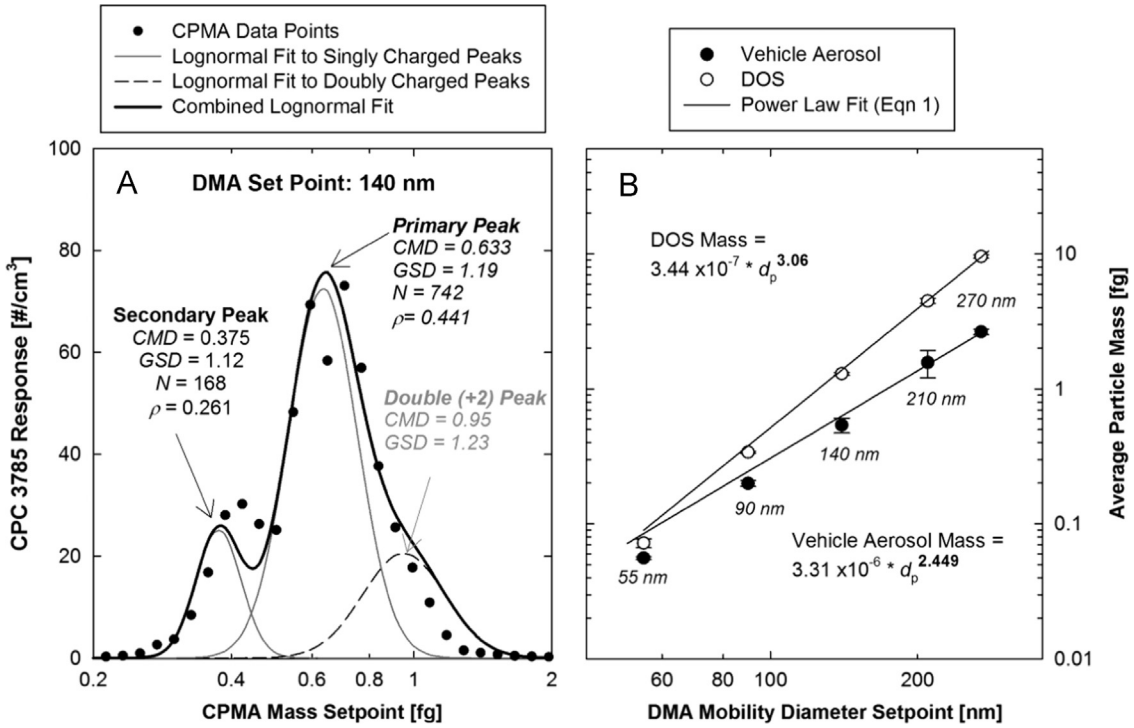


**Fig. 3.** Lognormal fitting procedure of CPMA data for vehicle exhaust and laboratory-generated DOS. Shown in panel (A) is the mass spectrum at 140 nm during 16-kW SS operation of GDI-1 vehicle. The average mass calculated at each DMA set point is aggregated and shown in panel (B) for the same 16-kW test of GDI-1 and atomized DOS spheres.

sequence. In some cases, insufficient signal was generated ($<1.00$ particles/cm$^3$ reaching the CPC 3785) and no measurement was completed.

Average particle mass was determined from CPMA spectra as shown in Fig. 3, where multimodal lognormal fitting was conducted using DistFit 2009 (Chimera Technologies, Inc., Forest Lake, MN, USA) to calculate the average particle mass of all peaks corresponding to only particles carrying a single charge, $m_{p,i}$, for each DMA set point, $i$. The influence of doubly charged particles was removed by calculating the ratio of particle mass and concentration between doubly and singly charged particles transmitted by the DMA. This process involved determining the ratio between particle mobility diameter ($d_p$) carrying $i$ and $i+1$ charges, which is a proportionality adapted from the definition of electrical mobility according to Hinds (1999) as follows:

$$\frac{d_{p,i+1}}{d_{p,i}} \propto \frac{C_{c,i+1}}{C_{c,i}} \frac{n_{i+1}}{n_i} \tag{1}$$

where $n$ equals the number of charges, and $C_c$ is the Cunningham slip correction factor. The ratio between the mobility equivalent volumes was used to calculate the ratio of the peaks as a function of CPMA mass set point. In addition, the relative concentration of doubly charged particles was calculated from the SMPS size distribution, and the positive charging efficiency of soot particles reported by Maricq (2008). This approach enabled both mass and concentration to be used to identify and remove the influence of doubly charged particles exiting the DMA that could influence results from the CPMA scan. This approach is similar to those described and implemented by Olfert et al. (2007) and Wang, Caldow, Sem, Hama, and Sakurai (2010) for estimating the doubly charged particle fraction, the latter of which has been adopted as an ISO standard (ISO/DIS 27891) for particle number measurement.

### 2.3.1. Accurate measurements at low concentrations

Maricq and Xu (2004) discussed the challenge of measurement particle effective density from PFI vehicles because concentrations are generally too low to be quantified using the DMA–ELPI method. When using the DMA–CPMA method, sufficient measurement signal was generated even for very dilute particle concentrations in CVS dilution air (200–500 #/cm$^3$) by using the TSI water-based CPC (model 3785, $d_{50}=5$ nm, Shoreview, MN) which provided 0.01 particles/cm$^3$ readability due to the highly sensitive laser optics and good counting statistics. Instead, the bigger challenge was distinguishing vehicle and dilution air signals at low concentrations. Whenever the vehicle emissions signal was less than five times higher than background, a separate CPMA scan was completed for the dilution air. Typically, background particle density was $\sim$1200 kg/m$^3$ irrespective of size, and peaks were clearly distinct from vehicle aerosol densities ($\sim$300–800 kg/m$^3$).

*2.3.2. Particle mass–mobility scaling exponent and effective density*

Schmidt-Ott, Baltensperger, Gäggeler, and Jost (1990) determined the mass of a particle, $m_p$, as a function of its mobility diameter $d_p$, mass constant $b$, and its mass–mobility scaling exponent $D_m$ assuming primary particle density as constant, as expressed by

$$m_p = b\, d_p^{D_m} \tag{2}$$

The mass–mobility scaling exponent expresses the change of particle mass with respect to mobility diameter according to nanoparticle aggregate theory of primary particle spherules (Lall & Friedlander, 2006; Sorensen, 2011).

Particle effective density, $\rho_{eff}$, is defined as the particle mass $m_p$ divided by the mobility equivalent spherical volume. Equation (3) shows the adapted equation for particle effective density from previous studies (e.g. McMurry et al., 2002; Olfert et al., 2007; Park et al., 2003; Skillas, Künzel, Burtscher, Baltensperger, & Siegmann, 1998):

$$\rho_{eff} = \frac{m_p}{(\pi/6)\, d_p^3} \tag{3}$$

Eqs. (2) and (3) then are combined to express particle effective density (kg/m$^3$) as a function of a new constant $c$ ($=6b/\pi$, a.u.), mobility diameter $d_p$ (nm), and mass–mobility scaling exponent $D_m$ as follows:

$$\rho_{eff} = 1000\, c\, d_p^{D_m - 3} \tag{4}$$

In order to properly determine the mass–mobility scaling exponent, agglomerates should have a reasonable number of monomers enabling an infinite number of conformations. Therefore, measurements at 30 nm were excluded from the fitting procedure used to obtain $D_m$, because the agglomerate size approaches within a factor of two primary particle diameter, which ranges between 10 and 25 nm for engine exhaust (Maricq & Xu, 2004; Wentzel, Gorzawski, Naumann, Saathoff, & Weinbruch, 2003). Fitted values of $D_m$ depend on flow regime, which in this study spanned the transition and continuum regimes (Sorensen, 2011). Therefore, in order to compare $D_m$ among operating conditions enabling a variable number of density measurements at unique DMA set points, this analysis is limited to the same five DMA set points between 55 and 270 nm inclusive. Table 2 reports fitted $D_m$ according to Eq. (2) and calculated $c$ according to Eq. (4) for each test condition using Pearson's least-squares regression.

Typically, fractal dimension is used to characterize the change of mass with size for a truly fractal agglomerate comprised solely of primary particle spherules. However, vehicle emissions contain solid primary particle spherules that are agglomerated during combustion and semi-volatile materials that condense onto solid particle cores during dilution and cooling. Therefore, the fitted mass–mobility scaling exponent characterizes the change of total particle mass (and density) with size. This approach is useful for defining effective density functions that can be used to estimate suspended PM mass.

The selection of an appropriate fitting method to the power law function is important because it determines the relative weighting of each mass point. The least squares regression used in this study minimizes total residuals, and because particle mass spanned about two orders of magnitude, greater weight is placed on larger particle sizes (DMA set point=270 nm) than on smaller particle sizes (DMA set point=55 nm). Some early vehicle exhaust studies (e.g. Ristimäki et al., 2002; Virtanen et al., 2002) used a method to weight particles by relative number abundance in the distribution; therefore reported fractal dimension (actually mass–mobility scaling exponent) weighted more heavily the smaller nucleation mode particles. Other fitting methods would be able to equally weight each point. However, this study used the least squares regression to allow larger particles to carry more weight because of their larger mass contribution when evaluating the IPSD method.

*2.3.3. EEPS vs. SMPS*

Particle size distribution (PSD) was measured over SS and ST conditions using an SMPS and two different units of the same EEPS model. The EEPS is carefully calibrated by the manufacturer using traceable PSL aerosol. However, its performance is uncertain particularly when measuring fractal engine exhaust containing a mixture of several chemical compounds (Asbach et al., 2009; Kaminski et al., 2013; Oh, Park, & Kim, 2004; Zimmerman et al., 2014). The EEPS does not adapt its inversion routine to account for differences in particle charging due to particle morphology. Therefore, in this study we compare the EEPS and SMPS distributions over a comprehensive range of conditions from a breadth of vehicle technologies. The Differential Mobility Spectrometer (DMS500, Cambustion Ltd.) does account for particle morphology effects on particle charging by calibrating the instrument with soot and PSL but it was not tested here.

We previously compared and corrected EEPS size distributions to an SMPS equivalent using a lognormal fitting approach described by Quiros et al. (2014). We believe the SMPS (Wang & Flagan, 1990) provides an accurate reference size distribution when proper transport and instrument response times are calculated between a calibrated DMA and CPC (Russell, Flagan, & Seinfeld, 1995). In this study, bimodal fits were derived from the average of the two EEPS size distributions and the SMPS distribution using the following three parameters for each mode $j$: the number of particles $N_j$, the geometric standard deviation $GSD_j$, and the count median diameter $CMD_j$. Then, the SMPS-to-EEPS ratio was calculated, and expressed as a third multimodal lognormal function. All lognormal fitting was also conducted using DistFit 2009 and

the form shown as follows:

$$Y = \frac{1}{\sqrt{2\pi}}\left[\sum_{1}^{j}\left[\frac{N_j}{\ln GSD_j} \times e^{-0.5\times[(\ln d_p - \ln CMD_j)/\ln GSD_j]^2}\right]\right] \quad (5)$$

where $N$, $GSD$, and $CMD$ are three constants derived by DistFit for the number of fitted peaks ($j$). The units of the ordinate $Y$ for initial EEPS or SMPS data were $dN/d\log d_p$, and the refitting of the SMPS-to-EEPS ratio was dimensionless.

## 3. Results

### 3.1. Particle mass–mobility scaling exponent and effective density

Figure 3(A) shows the lognormal fitting procedure used to determine average particle mass of 140-nm particles selected by the DMA during the 16-kW test of the GDI-1 vehicle. In this case, the CPMA scan reported three peaks: a primary peak centered at 0.633 fg with $\rho_{eff}=441$ kg/m$^3$, a secondary peak centered at 0.375 fg with $\rho_{eff}=261$ kg/m$^3$, and a doubly charged peak centered at 0.95 fg that was subtracted from the distribution before calculating average mass. In many cases, only two peaks were observed, a primary peak and its doubly-charged equivalent.

Fitting, using the power law described by Eq. (2), determined mass–mobility scaling exponents as illustrated in Fig. 3(B). One standard deviation of the measurement of each size is shown in the error bars. In Fig. 4, symbols represent measured data points, and best fit lines represent the fitting according to the power law model following Eq. (4). The fitted values for $D_m$ and $c$ are listed in Table 2 by engine operating condition.

#### 3.1.1. GDI-1 and GDI-2

The effective densities for GDI-1 and GDI-2 are plotted in Fig. 4(A) and (B), respectively. The emissions from GDI-1 had similar particulate effective density among all operation conditions, decreasing from ~700 kg/m$^3$ at 30 nm to ~200–300 kg/m$^3$ at 350 nm. In contrast, the particle effective density of GDI-2 particulate emissions was higher at 55 nm (900 kg/m$^3$) during 51-kW SS operation compared to all other conditions. However, particle effective density for 51-kW operation converged with other conditions for 270 nm and larger. When operating GDI-2 at higher engine speeds but maintaining constant power, particle effective density decreased between 10% and 20% for all sizes, and average mass–mobility scaling exponent decreased from either 2.52 (9-kW) or 2.47 (26-kW) to 2.40, resulting in lighter and less compact particles.

The effective densities of exhaust emissions from GDI-1 and GDI-2 were similar for smaller particles at 30 nm (650–800 kg/m$^3$) and also for larger particles at 350 nm (200–300 kg/m$^3$), despite differences in engine size (2.0-L versus 3.6-L) and PM emissions rates over the FTP cycle (0.99 versus 2.02 mg/mi (0.61 and 1.23 mg/km)). However, the mass–mobility scaling exponent of the emissions decreased to ~2.3 as power approached 100% of the calculated FTP maximum for both GDI-1 (30 kW) and GDI-2 (51 kW). The mass–mobility scaling exponents were significantly lower during these 100% FTP tests than any other GDI test when applying a two-sided Rank Sum Test for $\alpha=0.05$. It is possible that due to higher exhaust temperature, catalyst efficiency increased thereby reducing emissions of high molecular weight hydrocarbons and semi-volatile compounds to fill the soot void space. Up to this point, density measurements can be grouped as: (i) gasoline GDI, which thus far includes the average of GDI-1 and GDI-2 emissions, and (ii) the average of the 30-kW operation of GDI-1 and 51-kW operation of GDI-2, both operating at ~100% of FTP, hereafter, gasoline GDI FTP-max.

#### 3.1.2. PFI and PFI-E85

Figure 4(C) shows the effective densities measured from the gasoline PFI vehicle; these are the first reported densities from PFI engines in the literature. The trend of all the PFI density functions is similar to those from GDI emissions; namely, density decreases with increasing particle size from 600–700 kg/m$^3$ at 30 nm to 200–300 kg/m$^3$ at 350 nm for all conditions. However, important subtleties for PFI emissions are apparent from a careful analysis of the fitted mass–mobility scaling exponents. ST operation under lower load (5.4 kW) or SS operation under high load (18-kW) resulted in significantly higher ($\alpha=0.05$, two-sided Rank Sum Test) mass–mobility scaling exponents ($d_m=2.68$ and 2.67, respectively) than during 14-kW ST operation ($d_m=2.45$). These emissions from PFI engines are more spherical than GDI emissions, suggesting less soot formation as a result of homogenous fuel mixing during combustion. Because the effective density was similar between 5.4-kW ST and 18-kW SS operation, when PM mass differed dramatically (0.01 versus 0.41 mg/mi, respectively, presented later in Fig. 9) over the 75-min cycle, the effect of ST operation alone is likely negligible on particulate effective density. The high loads elicited during 14-kW ST operation may have induced more heterogeneous fuel mixtures, which increased soot formation, resulting in the lower mass–mobility scaling exponent. It should be pointed out that only the combination of high load and ST operation resulted in a lower mass–mobility scaling exponent, indicating that for the majority of transient driving, a generic PFI density function can be applied. Therefore a third new category of particle effective density will be defined: (iii) PFI gasoline, the average of the 18-kW SS and 5.4-kW ST conditions.

Figure 4(D) shows the effective densities measured from the PFI-E85 vehicle were lower than the PFI gasoline vehicle for all sizes. However, the trends between the two vehicles were similar. Nucleation mode particles measured at 30 nm were roughly equivalent to the effective densities measured at 55 nm, between 500 and 600 kg/m$^3$, and particle effective density was a decreasing function of particle diameter reaching 200–300 kg/m$^3$ at 270 nm. Unlike the PFI gasoline particle effective

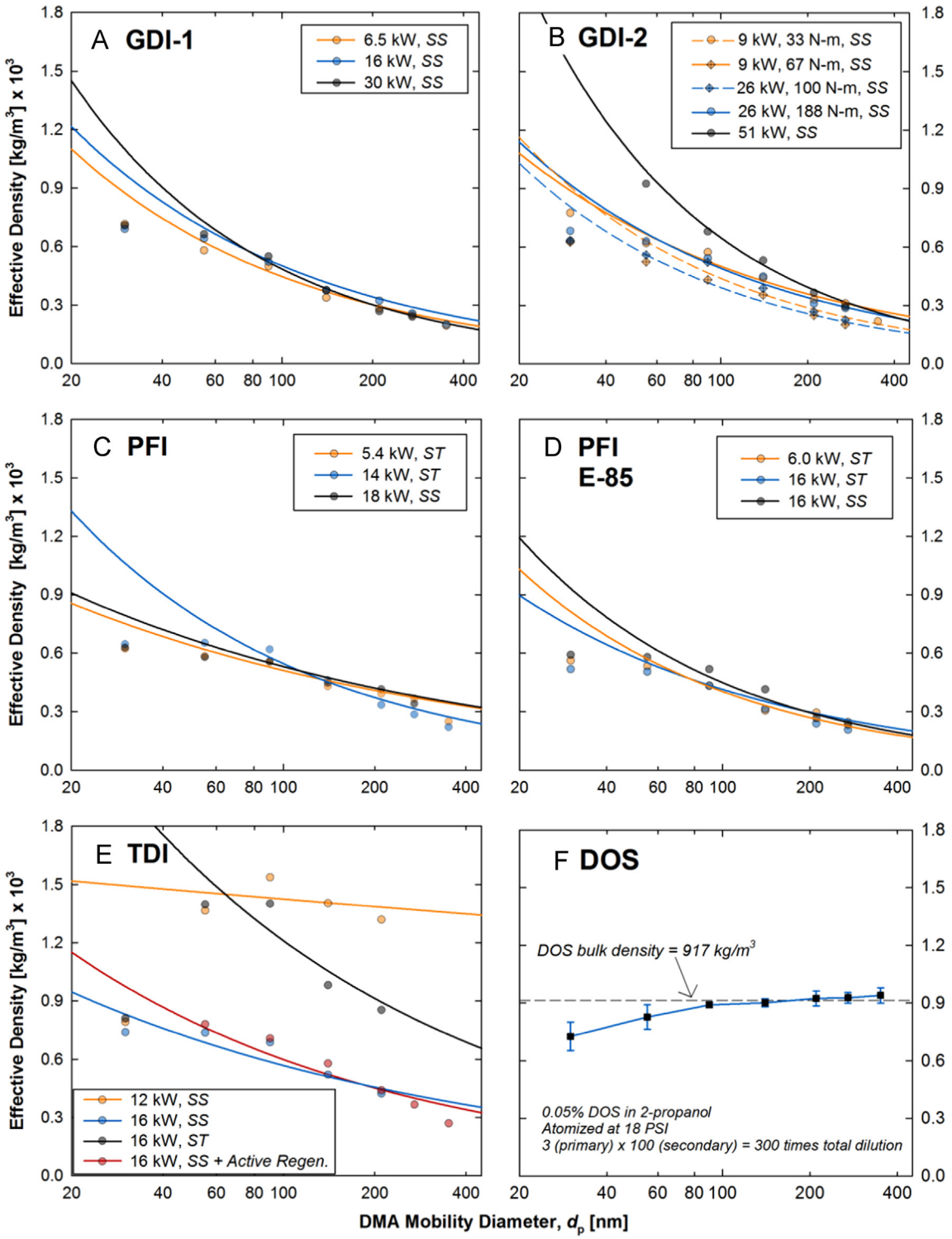


**Fig. 4.** Fitted particle effective density functions and raw data points by condition as a function of electrical mobility diameter for (A–E) the five light-duty vehicles and (F) the atomized DOS.

density functions, the calculated density curves from the PFI-E85 were not a strong function of operation condition, where mass–mobility scaling exponent of vehicle exhaust from the PFI-E85 ranged from ~2.4 to 2.5. Although the PFI-E85 vehicle does not use direct fuel injection, the mass–mobility scaling exponent was more comparable to GDI emissions, and the

**Table 3**
Coefficients for average gasoline particle effective density functions shown in Fig. 5(a).

| | (i) Gasoline GDI | (ii) Gasoline GDI FTP-max | (iii) Gasoline PFI | (iv) Gasoline PFI-E85 |
|---|---|---|---|---|
| Exponent, $D_m$ | $2.45 \pm 0.05$ | $2.30 \pm 0.02$ | $2.67 \pm 0.01$ | $2.44 \pm 0.07$ |
| Constant, $c$ | 6.0 | 14 | 2.4 | 6.0 |

particle effective density function was lower than PFI and GDI emissions. Therefore, its particle effective density function is grouped into a fourth category (iv): PFI-E85, the average of 6-kW ST, 16-kW ST, and 16-kW SS operations.

### 3.1.3. TDI

Figure 4(e) presents the effective densities calculated from the TDI vehicle, also the first time in the literature particle effective density has been measured downstream of a DPF. For two of the three conditions (12-kW SS and 16-kW ST), effective densities were dramatically greater than for all other conditions; the effective densities ranged between 900 and 1600 kg/m$^3$ between 30 and 210 nm. During 12-kW SS operation (87% of FTP), the mass–mobility scaling exponent was $2.96 \pm 0.04$, indicating nearly spherical particles. The high mass–mobility scaling exponent suggests the DPF effectively removes fractal-like soot, where remaining particles are solid refractory particles or those formed by nucleation of higher molecular weight semi-volatile materials downstream of the DPF as has been shown in heavy-duty applications (e.g. Biswas et al., 2008; Kittelson et al., 2006). Under an increased vehicle load during 16-kW SS and 16-kW ST operation (92% of FTP), mass–mobility scaling exponent decreased to $\sim$2.6, possibly due to the passage of fractal soot agglomerates due to diminished DPF filtration efficiency or higher engine soot production. However, particle effective density remained higher during ST operation (900–1400 kg/m$^3$) than during SS operation (300–800 kg/m$^3$) at the same power output.

An active DPF regeneration was triggered automatically by the engine control module for an approximate 10–20 min period during each of the 16-kW SS test cycles in this study (approximately every 320 km). The active regeneration event was characterized by an increase in oxidation catalyst temperature from 270 to 490 °C, which resulted in CVS particle number concentration increasing by two to three orders of magnitude. Interestingly, active regeneration occurred during the 16-kW SS operation and produced a particle effective density which is nearly equivalent to our observation during the 16-kW SS operation without active regeneration.

### 3.1.4. Literature comparison: gasoline vehicles

As presented in the previous section, particle effective densities for gasoline vehicles are grouped into four relevant and statistically significant groups: (1) gasoline GDI, defined by all measurements from GDI-1, GDI-2 except those denoted hereafter, (2) gasoline GDI FTP-max, defined by arithmetic mean density measured 30-kW SS operation of GDI-1 and 51-kW SS operation of GDI-2, (3) gasoline PFI, defined by the arithmetic mean of the 5.4-kW ST and 18-kW SS operation, and (4) PFI-E85, defined by the arithmetic mean of all three test conditions of the vehicle. Table 3 presents these parameters for calculating particle effective density using mass–mobility scaling exponent and the defined constant in Eq. (4).

The widely recognized evaluation of gasoline particle effective density was conducted by Maricq and Xu (2004) using a Direct Injection Spark Ignition, or DISI vehicle, which is now known as GDI. The authors reported a mass–mobility scaling exponent of $2.3 \pm 0.1$ using the DMA–ELPI method for a range of operating conditions. The curves shown in Fig. 5(A) for gasoline emissions were plotted using mass–mobility scaling exponents of 2.2 and 2.4 while $c$ was determined iteratively until the value calculated for 60 nm equaled the graphically presented data in the literature. All measurements of emission from gasoline vehicles in this study show a lower density at 55 nm (600–800 kg/m$^3$) than those reported by Maricq and Xu (2004). The density at larger particle sizes closely matches for all conditions (gasoline GDI, gasoline GDI FTP-max, and gasoline E85) except for gasoline PFI, which demonstrated a higher mass–mobility scaling exponent and therefore greater particle effective density for larger sizes.

Figure 5(A) also plots the density function, which Liu et al. (2009) presented as an exponential fit to Maricq and Xu (2004) data. The exponential fitting process provides a smooth transition between the flat density function of nucleation-mode particles to the power law decay empirically fit to larger fractal-like particles. However, the exponential fit model deviates from measured data at larger sizes and underestimates the particle effective density, whereas the power fit law provided good fit to experimental data up to 350 nm. This underestimation provides some explanation of the underestimation of PM mass for our initial evaluation of the IPSD method (Li et al., 2014).

### 3.1.5. Literature comparison: diesel effective density

Figure 5(B) presents particle effective density measured for the TDI diesel equipped with a DPF and the data compared to other diesel engines without a DPF. Olfert et al. (2007) demonstrated higher DOC temperatures at high engine loads promotes homogenous nucleation of sulfate ($SO_2$ to $SO_3$ conversion), which condenses onto fractal agglomerates and increases mass–mobility scaling exponent: $d_m = 2.76$ at 40% compared to $d_m = 2.36$ at 15% load of the same light-duty diesel vehicle. Maricq and Xu (2004) reported $d_m = 2.3$ from testing of another light-duty diesel vehicle at 64 and 112 km/h, which ostensibly did not result in loads high enough to result in nucleation and condensation of sulfate because mass–mobility scaling exponent did not increase substantially when increasing vehicle load. Our measured effective densities and

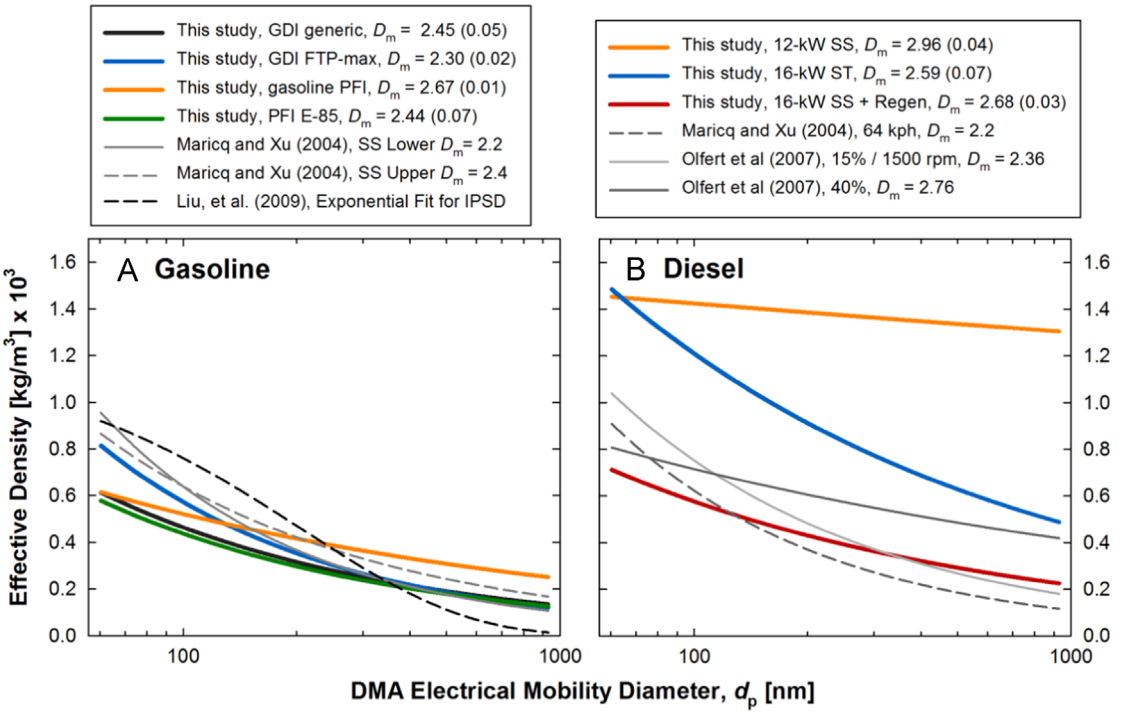


**Fig. 5.** Consolidated density functions for (A) gasoline and (B) diesel vehicles in this study compared to other selected studies.

mass–mobility scaling exponents were in agreement with previous evaluations only for the 16-kW SS operation, where density decreased from ~800 to 300 kg/m$^3$ between 55 and 270 nm according to $d_m$=2.59. The effective densities measured during 12-kW SS and 16-kW ST operation were notably higher than any previous evaluation, beginning around 1400 kg/m$^3$ at 55 nm and decreasing according to $d_m$=2.96 ± 0.04 and $d_m$=2.59 ± 0.02, respectively. The high particle effective density measured during 12-kW SS and 16-kW ST operations were not due to hydrated sulfate, because DOC temperature was only sufficiently high to promote $SO_2$ to $SO_3$ formation during active regeneration, which resulted ironically in the lowest effective densities equivalent to 16-kW SS operation.

### 3.2. Evaluation of IPSD over steady-state cycles

#### 3.2.1. Derivation of SMPS-to-EEPS ratios

Figure 6(A) shows the lognormal fitting procedure used to quantitatively relate EEPS and SMPS size distributions. A bimodal fit was applied to each distribution in order to segregate the smaller nucleation mode particles (diameter 10–30 nm) from the larger accumulation mode particles (diameter > 30 nm) that are expected to have different physical properties producing measurement bias between the two instruments. Figure 6(B) shows the SMPS-to-EEPS ratios for each vehicle, averaged over all operating conditions evaluated. The ratios were impacted by operating condition, most especially TDI emissions. The average for each vehicle is presented, and the average of all the vehicles is shown by the thick solid black line. The average of all test conditions can be quantitatively expressed using Eq. (5) and the following inputs derived from the data $N_1$=0.99, $N_2$=1.9, $N_3$=20, $GSD_1$=1.5, $GSD_2$=3.0, $GSD_3$=1.9, $CMD_1$=19, $CMD_2$=56 and $CMD_3$=750.

Based on the study-average function, the EEPS overestimated particle concentrations from 20 to 100 nm, and underestimated smaller and larger particles. These results are strikingly similar to a recent evaluation by Zimmerman et al. (2014) who reported EEPS overestimation at 20 and 120 nm relative to the SMPS when measuring diesel exhaust. The underestimation of larger particles between 100 and 560 nm is important, for these particles contribute greater particle mass than smaller particles, and therefore this issue would need to be addressed when applying IPSD. Therefore, the five functions shown in Fig. 6(B) were applied to correct EEPS data to evaluate the improvement by correcting to an SMPS equivalent.

#### 3.2.2. Size distributions

Figure 7 presents the mass distributions based on corrected EEPS, SMPS, and APS distributions during two selected tests. For graphical purposes only, the mobility and aerodynamic diameters were combined using a similar approach discussed by Khlystov, Stanier, and Pandis (2004) using particle effective density functions measured in this study to convert

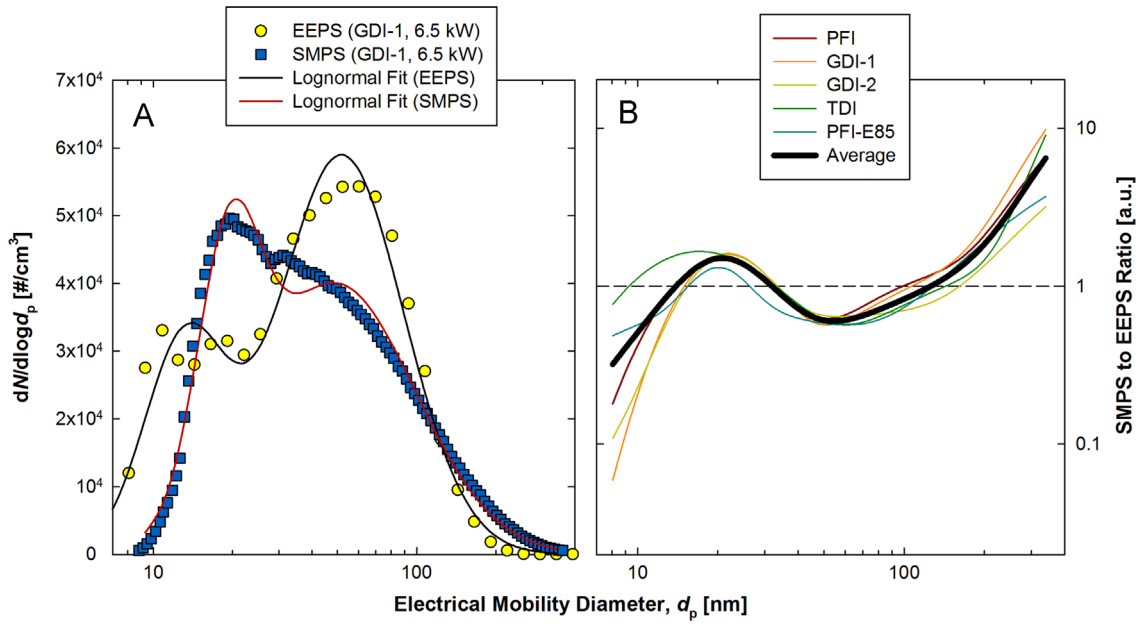


**Fig. 6.** (A) The bimodal fitting approach for comparing the size distributions measured by the SMPS and the EEPS, and (B) the average SMPS-to-EEPS ratios as a function of mobility diameter.

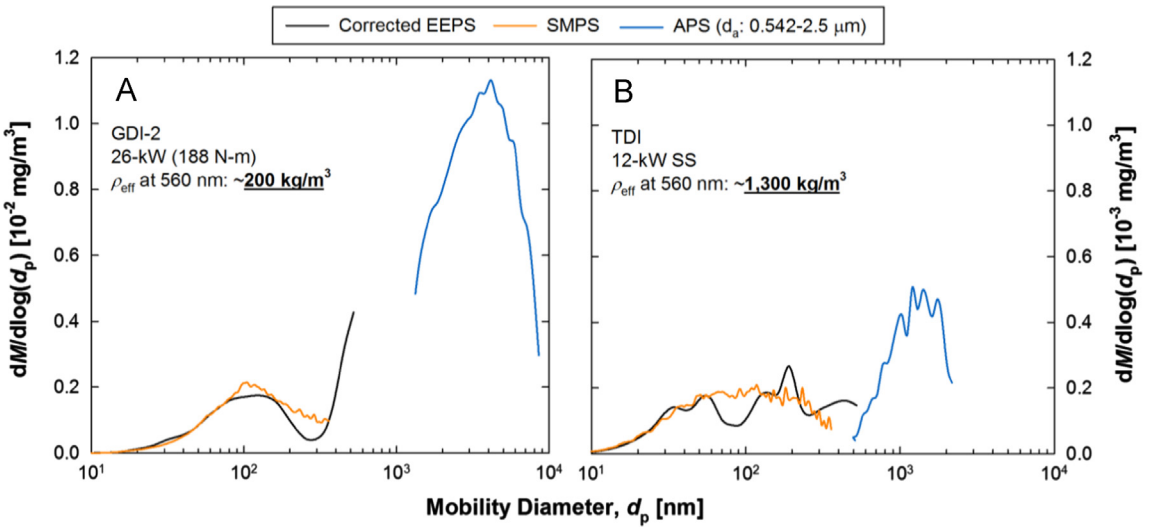


**Fig. 7.** Particle mass distributions shown from the corrected EEPS, SMPS, and APS where particle effective density is (A) less than 1000 kg/m$^3$ and (B) greater than 1000 kg/m$^3$ at 560 nm.

aerodynamic distributions to a mobility diameter equivalent using

$$\rho_e(d_p)\, d_p^2\, C_c(d_p) = \rho_0(d_a)\, d_a^2\, C_c(d_a) \tag{6}$$

where $d_p$ is the mobility diameter as previously defined, $d_a$ is the aerodynamic diameter, $C_c$ is the Cunningham slip correction factor as a function of respective diameter, and $\rho_0$ is unit density according to the definition of aerodynamic diameter.

Figure 7(A) presents size distributions measured by the EEPS and APS during 26-kW (188 N m) operation of GDI-2. In this case, particle effective density at 560 nm ($\sim$200 kg/m$^3$) was lower than unit density (1000 kg/m$^3$), and the APS range ($d_a$=0.54–2.5 μm) becomes extended to 1300–8600 nm when converted into mobility diameter. This illustrates a gap between measurement ranges and that some PM is not sampled by either measurement approach. For other conditions as shown in Fig. 7(B) for the 12-kW SS operation of the TDI diesel vehicle, particle effective density at 560 nm (1200–1300 kg/m$^3$) is larger than unit density, and the referenced APS range is condensed to 510–2200 nm on a mobility scale. In this scenario, there is a

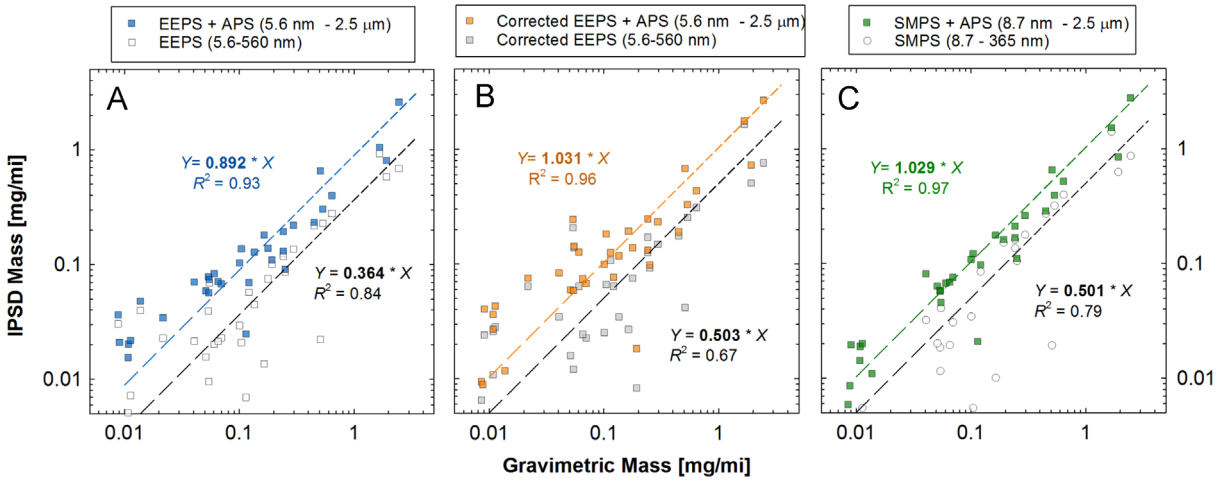


**Fig. 8.** Correlations of composite PM mass over the all 75-min test cycles measured by the IPSD method gravimetric method using (A) the EEPS and APS, (B) the EEPS with correction and APS, and (C) the SMPS and APS. No intercepts were used in determining best fit linear lines.

theoretical small overlapping measurement range. Therefore for simplicity, the contribution of larger particles is calculated by the sum of the aerodynamic fraction measured by the APS between 0.54 and 2.5 μm, and the mobility fraction measured by the EEPS or SMPS. Accordingly, the conversion of aerodynamic diameter to mobility diameter with Eq. (6) is merely to graphically illustrate the overlap or gap in the measurement ranges shown in the figure.

### 3.2.3. *Correlation with gravimetric method*

Gravimetric filter samples were collected to evaluate the IPSD method over SS and ST cycles using (A) uncorrected EEPS data, (B) corrected EEPS data, and (C) SMPS data shown in Fig. 8. Uncorrected EEPS data show the best correlation to gravimetric data ($R^2$=0.84), followed by SMPS ($R^2$=0.79) then corrected EEPS data ($R^2$=0.67). However, the IPSD method persistently underestimated gravimetric PM mass by 50–64% as shown by the slope of the black dashed lines in each panel. When considering the contribution of larger particles between 0.54 and 2.5 μm in aerodynamic diameter measured by the APS ($\rho_0$=1000 kg/m$^3$, by definition), bias was virtually eliminated between gravimetric and IPSD methods using corrected EEPS+APS distributions (slope=1.031) and SMPS+APS distributions (slope=1.029). Good fit was achieved when combining either corrected EEPS or SMPS with APS measurements ($R^2$=0.96 and 0.97); however, visual scatter in the low measurement range ( < 0.3 mg/mi/0.18 mg/km) was greater for the corrected EEPS data shown in Fig. 8(B) compared to the SMPS data shown in Fig. 8(C). Nevertheless, corrected EEPS data showed reduced measurement bias against the gravimetric method compared to the uncorrected data (slope=1.031 versus 0.892), suggesting some measurement improvement when applying the empirically derived correction ratio.

No positive or negative residuals were observed in the correlation between the gravimetric and IPSD methods down to at least 0.1 mg/mi (0.06 mg/km) as shown in Fig. 8(C) for the SMPS+APS. This suggests filter loadings were dominated by particle-phase emissions during the 75-min steady-state tests conducted in this study, and is consistent with IPSD tunnel blank calculations. The suspended mass contributions in the dilution air affecting IPSD detection limit were calculated based on SMPS (constant $\rho_{eff}$=1200 kg/m$^3$) and APS (unit density) data during tunnel blank procedures, resulting in a calculated suspended mass concentration of ~0.6 μg/m$^3$, which equates to 0.014 ± 0.010 mg/mi (0.0087 ± 0.0062 mg/km) over the SS and ST sequences. Nevertheless, gaseous adsorption may still impact filter measurement variability, especially during transient FTP certification tests that are of shorter duration (~32 min for a three-phase test).

### 3.2.4. *Size fraction mass contributions*

Figure 9 presents the size fractional contributions during the steady-state and single FTP tests by the following delineations: mobility diameters of 5.6–100 nm, 100–340 nm, and 340–560 nm based on corrected EEPS data, and aerodynamic diameters between the nominal 560 nm and the 2.5 μm APS. The average filter-based PM emissions factors for each cycle are indicated above each column for reference.

The smallest size fraction (5.6–100 nm) indicates the mass contribution from ultrafine PM, which contributed less than 25% of total mass in most cases. This fraction was substantially greater (~65%) during 51-kW SS test of GDI-2, where a dominant nucleation mode was observed. The ultrafine PM mass contribution was less than 5% for all tests conditions of the PFI-E85, including the single FTP test. Otherwise, there was no trend associated between operating conditions or vehicle engine load and the contribution from ultrafine PM.

The largest size fraction (560 nm–2.5 μm) measured by the APS varied dramatically between 2% and 80%. There was variability between the two GDI vehicles evaluated over steady-state cycles; the fractional contributions ranged 10–40% for GDI-1 and 25–72% for GDI-2. The largest fraction was observed for the 16-kW ST operation of the PFI-E85 vehicle.

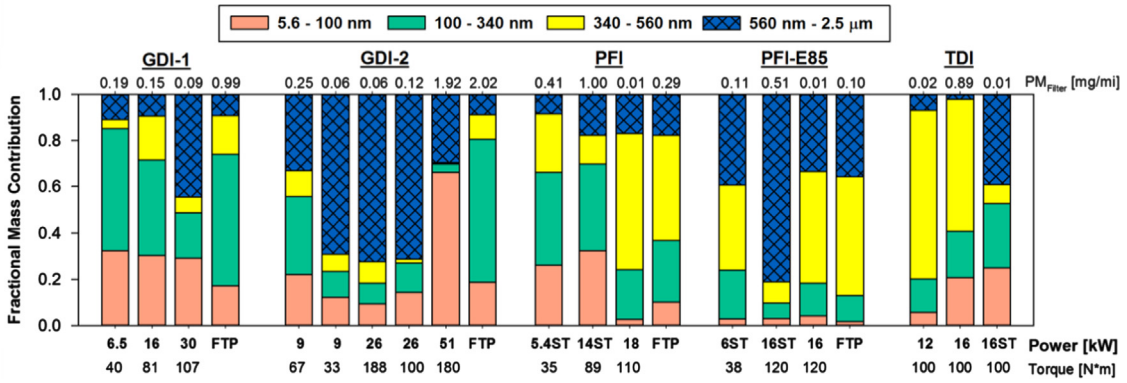


**Fig. 9.** The relative contribution of PM mass defined by four relative size fractions measured by corrected EEPS data under each steady-state and transient (FTP) vehicle test.

The contribution of larger particles was minimal from the DPF-equipped TDI diesel vehicle, even during active regeneration, in contrast to our previous work for heavy-duty diesel regeneration (Quiros et al., 2014). However, the larger particles were observed during 16-kW ST operation, where the removal efficiency of the DPF may have declined during higher bursts of exhaust flow. This observation is consistent with the decreased mass–mobility scaling exponent observed from the density function. During each of the single FTP tests, the fractional contribution of larger PM beyond the EEPS measurement range ranged between 9% and 35%.

## 4. Discussion and conclusion

Particle effective density functions were derived from measurements between 55 and 270 nm. Measured data for larger sizes (i.e. 350 nm) fit to the power law model well, and therefore, the parameters can be used to estimate particle effective density for larger mobility diameters. For smaller particles, effective density typically plateaus, and in some cases, increases between 30 and 55 nm. Further investigation could help better understand this increase; for example a thermodenuder could be used to examine the influence of organic and sulfate concentrations on particle effective density and mass–mobility scaling exponent. Therefore, as a general rule, the authors recommend using the calculated value at 55 nm for smaller particles.

The effective densities of the four gasoline vehicles tested in this study (i.e. two GDI, a PFI, and a flex-fuel PFI operating on E85) were largely consistent with the first evaluation of GDI emissions made by Maricq and Xu (2004). These results suggest gasoline particle effective density functions may continue to remain robust to evolving emissions reduction strategies, and can be used for accurately measuring mass emissions from future generations of vehicles that are not equipped with gasoline particulate filters. Each particle effective density function is summarized by a power law model (Eq. (4)) and coefficients are listed in Table 3. The dataset of gasoline density functions is reduced into four summary functions: gasoline GDI, gasoline GDI FTP-max, gasoline PFI, and gasoline PFI-E85. Except for at the highest loads evaluated for each gasoline vehicle (Table 2), effective density is a stronger function of vehicle technology than vehicle load and steady state (SS) versus simulated-transient (ST) operation. Therefore, these four effective density functions for gasoline vehicles can be generally applied to vehicles using similar engine technologies over a range of steady-state or transient operations, for any vehicles certified inside or outside of the California market using similar emissions control strategies.

Particle effective density functions measured from the TDI vehicle are reported by the conditions listed in Table 2 rather than averaging or reporting of universal functions. Effective density for the TDI was a strong function of vehicle load; therefore, additional measurements should be conducted using a larger sample of DPF-equipped light-duty diesel vehicles. Importantly, the TDI vehicle was procured new and therefore had a very low odometer reading of 320 km after undergoing preparation procedures. The accumulation and release of sulfur compounds has been documented to occur during field aging of diesel after treatment devices (Herner et al., 2011; Swanson et al., 2009). Therefore, the emission of hydrated sulfate during active regeneration periods where DOC temperature was sufficiently high may result in elevated particle effective density ($\sim$1500 kg/m$^3$) for nucleation mode particles (Zheng et al., 2011). Although our density functions were measured near these values, during active regeneration periods when catalyst temperature was sufficient to promote sulfate nucleation, lower density functions were measured. Therefore, caution should be exercised when applying these particle density functions to vehicles with higher quantities of accumulated mileages, such as during the useful life period.

Good linear correlation was found between the gravimetric and IPSD methods when applying the new particle effective density functions to size distribution measured by the EEPS ($R^2$=0.84); however, the IPSD method underestimated gravimetric mass by 64%. When using the APS to measure the contribution of larger particles between 0.54 and 2.5 μm aerodynamic diameter, measurement bias between the methods was lowered to less than 3%, and fit improved dramatically ($R^2$=0.96). Even stronger correlation between ISPD and gravimetric methods was achieved, with little measurement bias

when using the SMPS instead of the EEPS with the APS ($R^2=0.97$). The good agreement of IPSD and gravimetric methods has previously been shown by Liu et al. (2012), but our results indicate that approximately half of PM mass lay within the SMPS range (8.7–365 nm). Liu et al. (2012) configured their SMPS to measure particles over a wider range, 15–660 nm, and in addition, calculated PM mass between 10 and 1000 nm by applying a lognormal fit equation. In principle, we uphold the validity of this fitting method; however, the actual measurement of size distributions provides a better measure of particulate mass than estimation by lognormal fit models.

In Fig. 6, we compare SMPS and EEPS size distributions using lognormal fitting curves over all the SS and ST cycles in this study. As a proof of concept refining the EEPS inversion method, we corrected our EEPS data to an SMPS equivalent using these empirically derived equations. Measurement bias between IPSD and gravimetric methods was reduced using the corrected versus uncorrected EEPS; however, increased scatter was observed for tests emitting less than 0.3 mg/mi (0.18 mg/km). Future work could evaluate the Cambustion DMS, which is commercially available and has been calibrated directly using fractal-like vehicle PM. The contribution of larger particles measured by the APS could be further evaluated using a Dekati ELPI to measure smaller and larger particles up to 10 μm using a single aerodynamic distribution. However, similar to the EEPS, both the DMS and the ELPI utilize electrometer signals to calculate concentration, and therefore could have some fundamental limitations to measurement of particle size distributions for determination of suspended mass.

In summary, this work presents particle effective density functions from two late model year GDI vehicles, and for the first time, two PFI vehicles, and a diesel passenger car equipped with a DPF. Over the SS and ST cycles measured, gravimetric and IPSD methods exhibited excellent agreement for steady-state emissions over the emission ranges evaluated ($R^2 > 0.96$). Virtually no measurement bias was observed between the methods when combining measurements from an EEPS or SMPS with an APS to capture particle emissions up to 2.5 μm. These data underscore the importance of defining measurement size range when performing real-time PM measurement. Moreover, these results are based on the measurement of steady-state emissions, and the IPSD method should be re-evaluated over transient test cycles.

## Acknowledgments

The authors thank the ARB management and staff who assisted during the project plan development and provided laboratory assistance during testing including Mark Fuentes, Wayne McMahon, M.-C. Oliver Chang, Sherry Zhang, Bruce Frodin, William Robertson, Henry Toutoundjian, Manuel Cruz, Derrick Lee, Huy Khou, and Inna Dzhema. The authors also thank Matti Maricq of Ford Motor Company for his feedback in the design of the test program. The statements and opinions expressed in this paper are solely the authors' and do not represent the official position of ARB. The mention of trade names, products, and organizations does not constitute endorsement or recommendation for use. ARB is a department of the California Environmental Protection Agency. ARB's mission is to promote and protect public health, welfare, and ecological resources through effective reduction of air pollutants while recognizing and considering effects on the economy. ARB oversees all air pollution control efforts in California to attain and maintain health-based air quality standards.

## References

Ahlvik, P., Ntziachristos, L., Keskinen, J., & Virtanen, A. (1998). Real-time measurements of diesel particle size distribution with an electrical low-pressure impactor, SAE 98-0410. *SAE Transactions*, *107*, 95–113.

Asbach, C., Kaminski, H., Fissan, H., Monz, C., Dahmann, D., & Mülhopt, S., et al. (2009). Comparison of four mobility particle sizers with different time resolution for stationary exposure measurements. *Journal of Nanoparticle Research*, *11*, 1593–1609.

Barone, T.L., Lall, A.A., Storey, J.M.E., Mulholland, G.W., Prikhodko, V.Y., & Frankland, J.H., et al. (2011). Size-resolved density measurements of particle emissions from an advanced combustion diesel engine: Effect of aggregate morphology. *Energy & Fuels*, *25*, 1978–1988.

Biswas, S., Hu, S., Verma, V., Herner, J.D., Robertson, W.H., & Ayala, A., et al. (2008). Physical properties of particulate matter (PM) from late model heavy-duty diesel vehicles operating with advanced PM and NO*x* emission control technologies. *Atmospheric Environment*, *42*, 5622–5634.

Bullock, D.S., & Olfert, J.S. (2014). Size, volatility, and effective density of particulate emissions from a homogeneous charge compression ignition engine using compressed natural gas. *Journal of Aerosol Science*, *75*, 1–8.

CARB (2012a). *Development of particulate matter mass standards for future light-duty vehicles*. Technical support document (Vol. Appendix P, 165 pp.).

CARB (2012b). *Procedure for preparation and handling of aerosol sampling media*. California Air Resources Board, Monitoring and Laboratory Division.: .

Ehara, K., Hagwood, C., & Coakley, K.J. (1996). Novel method to classify aerosol particles according to their mass-to-charge ratio—Aerosol particle mass analyser. *Journal of Aerosol Science*, *27*, 217–234.

EPA, U.S. (2002). Health assessment document for diesel engine exhaust. EPA/600/8-90/057F. United States Environmental Protection Agency.

Herner, J.D., Hu, S., Robertson, W.H., Huai, T., Chang, M.C.O., & Rieger, P., et al. (2011). Effect of advanced aftertreatment for PM and NO*x* reduction on heavy-duty diesel engine ultrafine particle emissions. *Environmental Science & Technology*, *45*, 2413–2419.

Hill, J., Polasky, S., Nelson, E., Tilman, D., Huo, H., & Ludwig, L., et al. (2009). Climate change and health costs of air emissions from biofuels and gasoline. *Proceedings of the National Academy of Sciences*, *106*, 2077–2082.

Hinds, W. C. (1999). *Aerosol technology, properties behavior and measurement of airborne particles* (2nd ed.).

Hu, S., Zhang, S., Sardar, S., Chen, S., Dzhema, I., Huang, S.-M., et al. (2014). *Evaluation of gravimetric method to measure light-duty vehicle particulate matter emissions at levels below one milligram per mile* (*1 mg/mile*). Paper 2014-01-1571. SAE Technical Paper.

Johnson, T.J., Symonds, J.P.R., & Olfert, J.S. (2013). Mass–mobility measurements using a centrifugal particle mass analyzer and differential mobility spectrometer. *Aerosol Science and Technology*, *47*, 1215–1225.

Kaminski, H., Kuhlbusch, T.A.J., Rath, S., Götz, U., Sprenger, M., & Wels, D., et al. (2013). Comparability of mobility particle sizers and diffusion chargers. *Journal of Aerosol Science*, *57*, 156–178.

Kelly, W.P., & McMurry, P.H. (1992). Measurement of particle density by inertial classification of differential mobility analyzer-generated monodisperse aerosols. *Aerosol Science and Technology*, *17*, 199–212.

Keskinen, J., Pietarinen, K., & Lehtimäki, M. (1992). Electrical low pressure impactor. *Journal of Aerosol Science*, *23*, 353–360.

Khlystov, A., Stanier, C., & Pandis, S.N. (2004). An algorithm for combining electrical mobility and aerodynamic size distributions data when measuring ambient aerosol (Special issue of aerosol science and technology on findings from the fine particulate matter supersites program). *Aerosol Science and Technology*, *38*, 229–238.
Kittelson, D.B., Watts, W.F., Johnson, J.P., Rowntree, C., Payne, M., & Goodier, S., et al. (2006). On-road evaluation of two diesel exhaust aftertreatment devices. *Journal of Aerosol Science*, *37*, 1140–1151.
Lall, A.A., & Friedlander, S.K. (2006). On-line measurement of ultrafine aggregate surface area and volume distributions by electrical mobility analysis: I. Theoretical analysis. *Journal of Aerosol Science*, *37*, 260–271.
Lehmann, U., Niemelä, V., & Mohr, M. (2004). New method for time-resolved diesel engine exhaust particle mass measurement. *Environmental Science & Technology*, *38*, 5704–5711.
Li, Y., Xue, J., Johnson, K., Durbin, T., Villela, M., Pham, L., et al. (2014). *Determination of suspended exhaust PM mass for light-duty vehicles*, *2014-01-1594*. SAE technical paper.
Liu, Z., Swanson, J., Kittelson, D.B., & Pui, D.Y.H. (2012). Comparison of methods for online measurement of diesel particulate matter. *Environmental Science & Technology*, *46*, 6127–6133.
Liu, Z.G., Vasys, V.N., Dettmann, M.E., Schauer, J.J., Kittelson, D.B., & Swanson, J. (2009). Comparison of strategies for the measurement of mass emissions from diesel engines emitting ultra-low levels of particulate matter. *Aerosol Science and Technology*, *43*, 1142–1152.
Lloyd, A.C., & Cackette, T.A. (2001). Diesel engines: Environmental impact and control. *Journal of the Air & Waste Management Association*, *51*, 809–847.
Mamakos, A., Ntziachristos, L., & Samaras, Z. (2006). Evaluation of the Dekati mass monitor for the measurement of exhaust particle mass emissions. *Environmental Science & Technology*, *40*, 4739–4745.
Maricq, M.M. (2008). Bipolar diffusion charging of soot aggregates. *Aerosol Science and Technology*, *42*, 247–254.
Maricq, M.M., Podsiadlik, D.H., & Chase, R.E. (2000). Size distributions of motor vehicle exhaust PM: A comparison between ELPI and SMPS measurements. *Aerosol Science and Technology*, *33*, 239–260.
Maricq, M.M., & Xu, N. (2004). The effective density and fractal dimension of soot particles from premixed flames and motor vehicle exhaust. *Journal of Aerosol Science*, *35*, 1251–1274.
McMurry, P.H., Wang, X., Park, K., & Ehara, K. (2002). The Relationship between mass and mobility for atmospheric particles: A new technique for measuring particle density. *Aerosol Science and Technology*, *36*, 227–238.
Oh, H., Park, H., & Kim, S. (2004). Effects of particle shape on the unipolar diffusion charging of nonspherical particles. *Aerosol Science and Technology*, *38*, 1045–1053.
Olfert, J.S., & Collings, N. (2005). New method for particle mass classification—The Couette centrifugal particle mass analyzer. *Journal of Aerosol Science*, *36*, 1338–1352.
Olfert, J.S., Reavell, K.S., Rushton, M.G., & Collings, N. (2006). The experimental transfer function of the Couette centrifugal particle mass analyzer. *Journal of Aerosol Science*, *37*, 1840–1852.
Olfert, J.S., Symonds, J.P.R., & Collings, N. (2007). The effective density and fractal dimension of particles emitted from a light-duty diesel vehicle with a diesel oxidation catalyst. *Journal of Aerosol Science*, *38*, 69–82.
Park, K., Cao, F., Kittelson, D.B., & McMurry, P.H. (2003). Relationship between particle mass and mobility for diesel exhaust particles. *Environmental Science & Technology*, *37*, 577–583.
Pope, C.A., & Dockery, D.W. (2006). Health effects of fine particulate air pollution: Lines that connect. *Journal of the Air & Waste Management Association*, *56*, 709–742.
Quiros, D.C., Yoon, S., Dwyer, H.A., Collins, J.F., Zhu, Y., & Huai, T. (2014). Measuring particulate matter emissions during parked active diesel particulate filter regeneration of heavy-duty diesel trucks. *Journal of Aerosol Science*, *73*, 48–62.
Ristimäki, J., Virtanen, A., Marjamäki, M., Rostedt, A., & Keskinen, J. (2002). On-line measurement of size distribution and effective density of submicron aerosol particles. *Journal of Aerosol Science*, *33*, 1541–1557.
Russell, L.M., Flagan, R.C., & Seinfeld, J.H. (1995). Asymmetric instrument response resulting from mixing effects in accelerated DMA-CPC measurements. *Aerosol Science and Technology*, *23*, 491–509.
Schmidt-Ott, A., Baltensperger, U., Gäggeler, H.W., & Jost, D.T. (1990). Scaling behaviour of physical parameters describing agglomerates. *Journal of Aerosol Science*, *21*, 711–717.
Skillas, G., Künzel, S., Burtscher, H., Baltensperger, U., & Siegmann, K. (1998). High fractal-like dimension of diesel soot agglomerates. *Journal of Aerosol Science*, *29*, 411–419.
Sorensen, C.M. (2011). The mobility of fractal aggregates: A review. *Aerosol Science and Technology*, *45*, 765–779.
Swanson, J.J., Kittelson, D.B., Watts, W.F., Gladis, D.D., & Twigg, M.V. (2009). Influence of storage and release on particle emissions from new and used CRTs. *Atmospheric Environment*, *43*, 3998–4004.
Symonds, J.P.R., Reavell, K.S.J., & Olfert, J.S. (2013). The CPMA-electrometer system—A suspended particle mass concentration standard. *Aerosol Science and Technology*, *47* (i–iv).
U.S. EPA (2001). *Control of air pollution from new motor vehicles: Heavy-duty engine and vehicle standards and highway diesel fuel sulfur control requirements*. 40 CFR Part 69, 80, 86. Federal Register.
U.S. EPA (2012). *Vehicle-testing procedures*. 40 CFR 1066. Fedreal Register.
Van Gulijk, C., Marijnissen, J.C.M., Makkee, M., Moulijn, J.A., & Schmidt-Ott, A. (2004). Measuring diesel soot with a scanning mobility particle sizer and an electrical low-pressure impactor: Performance assessment with a model for fractal-like agglomerates. *Journal of Aerosol Science*, *35*, 633–655.
Virtanen, A., Ristimäki, J., & Keskinen, J. (2004). Method for measuring effective density and fractal dimension of aerosol agglomerates. *Aerosol Science and Technology*, *38*, 437–446.
Virtanen, A., Ristimäki, J., Marjamäki, M., Vaaraslahti, K., Keskinen, J., & Lappi, M. (2002). *Effective density of diesel exhaust particles as a function of size, 2002-01-0056*. SAE technical paper.
Virtanen, A.K.K., Ristimäki, J.M., Vaaraslahti, K.M., & Keskinen, J. (2004). Effect of engine load on diesel soot particles. *Environmental Science & Technology*, *38*, 2551–2556.
Wang, S.C., & Flagan, R.C. (1990). Scanning electrical mobility spectrometer. *Aerosol Science and Technology*, *13*, 230–240.
Wang, X., Caldow, R., Sem, G.J., Hama, N., & Sakurai, H. (2010). Evaluation of a condensation particle counter for vehicle emission measurement: Experimental procedure and effects of calibration aerosol material. *Journal of Aerosol Science*, *41*, 306–318.
Wentzel, M., Gorzawski, H., Naumann, K.-H., Saathoff, H., & Weinbruch, S. (2003). Transmission electron microscopical and aerosol dynamical characterization of soot aerosols. *Journal of Aerosol Science*, *34*, 1347–1370.
Zelenyuk, A., Cai, Y., Chieffo, L., & Imre, D. (2005). High precision density measurements of single particles: The density of metastable phases. *Aerosol Science and Technology*, *39*, 972–986.
Zelenyuk, A., Yang, J., Choi, E., & Imre, D. (2009). SPLAT II: An aircraft compatible, ultra-sensitive, high precision instrument for in-situ characterization of the size and composition of fine and ultrafine particles. *Aerosol Science and Technology*, *43*, 411–424.
Zheng, Z., Johnson, K.C., Liu, Z., Durbin, T.D., Hu, S., & Huai, T., et al. (2011). Investigation of solid particle number measurement: Existence and nature of sub-23 nm particles under PMP methodology. *Journal of Aerosol Science*, *42*, 883–897.
Zimmerman, N., Godri Pollitt, K.J., Jeong, C.-H., Wang, J.M., Jung, T., & Cooper, J.M., et al. (2014). Comparison of three nanoparticle sizing instruments: The influence of particle morphology. *Atmospheric Environment*, *86*, 140–147.